Influence of electrical potential on the crystallization and adhesion of potassium hydrogen tartrate crystals

Nadine Gabas, Maurice Comtat, Benjamin Huerta Ortega

Influence of electrical potential on the crystallization and adhesion of potassium hydrogen tartrate crystals

Benjamin Huerta-Ortega · Nadine Gabas · Maurice Comtat

Abstract Interfacial interactions between a hydroalcoholic solution of potassium hydrogen tartrate (KHT) and a stainless steel surface are studied, when an electrical potential is applied to the metal substrate. The capacitive domain of the metal–solution interface is determined by cyclic voltammetry. In order to study the influence of the potential on KHT nucleation and crystal adhesion, the solid–liquid interfacial energy is assessed from contact angle and capillary rise measurements. Experimentally, the contact angle between a NaF solution and a stainless steel vs. the potential has a parabolic behaviour. The metal topography has no apparent influence on physicochemical properties of the interface when ethanol is present in a KHT solution. The metal substrate promotes the formation of KHT crystals, which is improved by the application of an anodic potential. The adhesion of crystals becomes more effective when wires of 25 μm diameter are used in comparison with those of 250 μm.

Keywords Electrified interface · Interfacial energy · Contact angle · Capillary rise · Wetting · Electrocapillarity

1 Introduction

The crystallization of tartaric acid salts in beverages is an undesirable phenomenon. In particular, the presence of ethanol in wine can cause the crystallization of potassium hydrogen tartrate (KHT) in bottles due to the reduction of KHT solubility during the winemaking process. However, KHT crystallization may be partly inhibited by natural components of grapes (proteins, polysaccharides, other colloids,…). Due to the complexity of these hydroalcoholic solutions obtained from the fermented grape juice, it is not yet possible to propose a universal preventive treatment for KHT crystallization before bottling. Considerable efforts have been devoted to kinetic studies of KHT nucleation and crystal growth [1–9] and different strategies to avoid this phenomenon have been proposed. One of them is the process called "cold trap", used in the nuclear industry for the purification of liquid sodium and adapted in the field of enology, which consists in crystallizing KHT on a 316L stainless steel wire grid at a low temperature [10]. The preliminary results have shown a kinetic enhancement of KHT crystallization. In addition, the crystallization rate is increased when an electrical potential in the range 0 to +0.4 V vs. a saturated calomel electrode is applied to the metal substrate. In these conditions, the formation of KHT crystals becomes more complex and depends on various physicochemical parameters.

Many efforts have been made in theoretical and experimental investigations to understand the role of physical properties of substrates in promoting crystallization through heterogeneous nucleation [11–29]. It is suggested that the reduction of the free energy of formation of a new solid phase on a solid substrate is due to molecular interactions that take place at the substrate–solution interface [11–13]. In the case of biomineralization, the ability of an

organic matrix substrate to nucleate mineral phases is closely related to the magnitude of the interfacial energy [17]. For example, calcium carbonate, phosphate and oxalate, are commonly involved in mineral deposits in specific anatomical locations in association with specific matrix components. From theoretical approaches made to connect the interfacial parameters with other ones measured by wettability, the Van Oss-Chaudhury-Good theory was applied to nucleation studies of inorganic crystals on organic substrates, which allows the prediction of how hydrophilic and hydrophobic interfacial forces may induce heterogeneous nucleation in various solvents [23]. Experimental descriptions of molecular interactions show that dispersive and polar Lifshitz-van der Waals forces are predominant during the induction period in homogeneous nucleation, while Lewis acid–base interactions are of major importance for the heterogeneous nucleation process [16, 24, 25]. However, other forces such as those involving the electrochemical double layer, due to the tendency of particular materials to acquire an electric charge when they are immersed in polar media, have not been taken into account in order to explain the measurements related to the surface properties of the substrate. In these cases, interfacial properties can vary by changing the electrostatic nature of the substrate or by applying an electric field which generates a normal force that promotes the wetting of a solid surface by a liquid. During crystallization, surfaces that are in contact with the solution may attract or repel the electrically charged crystal. These interactions of charged molecules alter their distribution inside the solution and lead to local nucleation. Numerous investigations indicate the important role of charged surfaces in nucleation phenomena [26–29]. According to these studies, nucleation and growth phenomena can be controlled or promoted by surface charge in order to stimulate electrostatic interactions, but a fundamental understanding of the structural and chemical parameters has not been provided.

On the other hand, the change of solid–liquid, liquid–vapour and solid–vapour interfacial energies by the application of an electrical potential was discovered and described by Lippmann in the nineteenth century [30]. However, only liquid metal–electrolyte interfaces were extensively studied. In the case of solid–liquid interfaces, many approaches have been tried to determine the interfacial energy from the double integration of the capacitance–potential curve obtained by impedance measurements. But the determination of the integration constants still remains unsolved. The first measurement of an interfacial energy at the solid–liquid interface was attempted by Frumkin et al. [31] using the captive bubble method. Recently, there has been interest in study of the wettability of solids by applying a potential. This has allowed quick development of the electrowetting phenomenon (modulation of the spreading of a liquid on a substrate by electrical potential differences) [32–39].

Since interfacial interactions and electrical modifications of the solid–liquid interface may influence KHT nucleation and crystal adhesion on the stainless steel wire grid, the main purpose of this work is to develop a strategy in order to access to molecular and mechanical interfacial interactions when the interface is electrically polarized. This information seems essential for understanding and establishing a correlation among the effect of interfacial energy, and nucleation and adhesion phenomena. Therefore, two kinds of experiments are presented in order to evaluate the effect of a low amplitude electrical potential on the spreading of a solution on a metal surface and on crystallization.

2 Experimental

2.1 Materials

Chemical reagents were of analytical grade. Sodium fluoride (NaF) and potassium sulfate (K_2SO_4) were obtained from Sigma-Adrich. Potassium hydrogen tartrate (KHT) was obtained from Prolabo. Electrolytic solutions (5×10^{-3} M NaF and 12.8×10^{-3} M KHT) were prepared from dissolution of salts in distilled water. A hydroalcoholic solution (12% vol. ethanol) containing 12.8×10^{-3} M KHT and 1.15×10^{-3} M K_2SO_4 was used in order to study the effect of ethanol on interfacial molecular interactions. The pH of each model solution was adjusted to a value of 3.8 with 0.5 M sulphuric acid or 2 M sodium hydroxide solution.

2.2 Electrochemical measurements

All electrochemical measurements were carried out using a VoltaLab model PGZ 100 potentiostat (Radiometer Analytical) driven by the VoltaMaster 4 software. The electrochemical cell consisted of three electrodes: Pt as the counter electrode, Ag/AgCl/saturated KCl electrode as the reference electrode and a working electrode. Four types of material (316L stainless steel, gold, platinum and glassy carbon) were used for the working electrode. A Luggin capillary was used to allow the contact between the reference electrode and the electrolytic solution. Before starting the measurements, all working electrodes were subjected to electrochemical surface pre-treatment which consisted in cyclic voltammetry performed in a 0.5 M H_2SO_4 solution at a scan rate of 150 mV s^{-1}. The potential limits were the beginning of the oxidation and reduction of water or protons, respectively. The pre-treatment was done until observation of reproducible voltammograms.

In all electrochemical experiments, solutions were deaerated with N_2 gas for 10 min and a N_2 flow above the solutions was maintained to avoid oxygen absorption from air. Cyclic voltammograms at a scan rate of 50 mV s^{-1} and at room temperature, were achieved.

2.3 Interfacial measurements

In the first method, solid–liquid interfacial energies of aqueous and hydroalcoholic solutions were estimated using the contact angle method. For this, a Digidrop GBX apparatus equipped with a CCD camera linked to a high quality Nikon optical device allowed the recording of 240 images per second. The images were treated and transmitted to a PC computer driven by the Win $Drop^{++}$ software. Electrolyte droplets were placed on the solid surface by an automatic injection system. The surface tension of each electrolyte was previously measured by the DuNouy method using a platinum ring and a Wilhelmy balance (Krüss tensiometer, Germany). The average values of five measurements of surface tension, at room temperature, were: 70.9×10^{-3} N m^{-1} for the NaF aqueous solution; 69×10^{-3} N m^{-1} for the KHT aqueous solution and 51×10^{-3} N m^{-1} for the KHT hydroalcoholic solution. In order to obtain information about the interfacial energy when the potential was applied, two flat plates separated by a sheet of paper wetted with a $CuSO_4$ solution (5×10^{-3} M) were placed horizontally on a flat holder of the Digidrop and connected to a DC power supply (Sefram 0−18 V, 1.2 A). Figure 1a shows the scheme of the installation used to study the influence of potential on the contact angle. When a constant potential difference was applied between the two electrodes, the potential between the upper flat plate and a reference electrode in contact with paper was determined. The potential of the upper flat plate was independent of time. The 316L stainless steel surface was washed before each use with 0.5 M H_2SO_4, rinsed thoroughly with distilled water and dried under air. Some determinations were achieved on a flat surface polished electrochemically. The electrochemical treatment consisted in using the 316L stainless steel plate as an anode in a solution containing 60% H_3PO_4, 30% H_2SO_4 and 10% H_2O with a current density of 300 mA cm^{-2} imposed for 30 min.

In the second method, capillary rise measurements were used to obtain information about the interfacial energy at the solid–liquid–vapour interface. In these experiments, the height of capillary rise was used to deduce contact angles in porous materials. Figure 1b illustrates the experimental set up. 316L stainless steel wires of 25 μm diameter were assembled to form a capillary structure. Before measurements, the capillaries were cleaned with 0.5 M H_2SO_4, rinsed with distilled water, dried, weighed, and placed on a

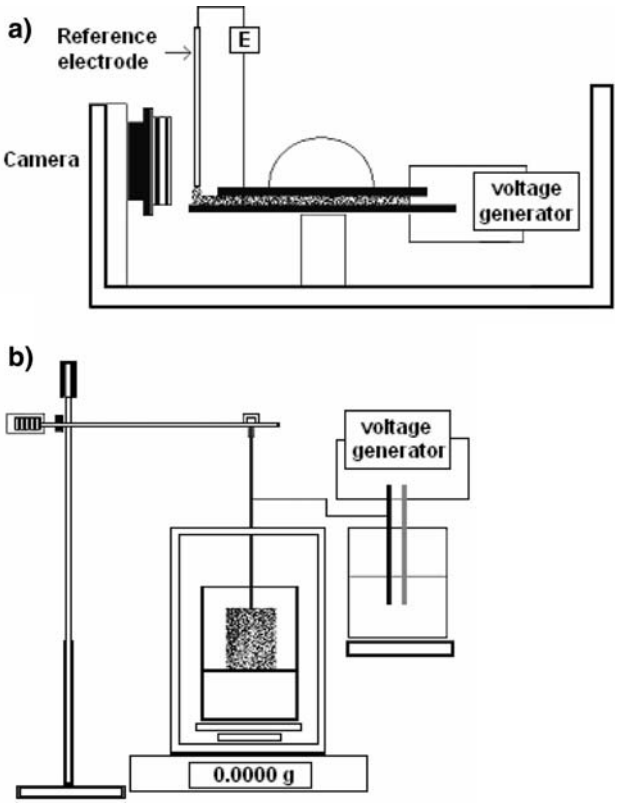

Fig. 1 Schemes of experimental devices for **a** wetting and **b** capillary rise measurements under the influence of potential

liquid surface. The electrolyte was contained in a glass which was placed on the tray of a high precision balance. The porous substrate was hung and connected to the support of a micrometric screw. In order to minimize evaporation, the solution and the porous substrate were contained in a closed vessel where the partial pressure was equal to the saturated vapour pressure of the solution at the working temperature. Wetting dynamics was followed from the moment when the capillary was put in contact with the surface of the electrolytic solution and the fast rise process was monitored by the mass variation with time. The experimental data were collected every second until the liquid reached an equilibrium value. The height of the solution was easily related to the mass of absorbed electrolytic solution, knowing its density.

2.4 Crystallization experiments

In KHT crystallization, the experimental procedure consisted in introducing 100 mL of the hydroalcoholic solution into the reactor and cooling it as quickly as possible until it reached the given temperature (11.5 °C). When the temperature was reached and remained constant during the test, the 316L stainless steel wire grid was

introduced into the reactor and a constant electrical potential was applied. The conductivity and temperature of the solution were recorded over the time. At the end of the experiment, the metal substrate was removed from the reactor, dried and weighed.

Two 316L stainless steel grids of different diameter were used to crystallize KHT: PF wires of 250 μm and PB wires of 25 μm diameter. Both substrates presented the same apparent surface which was evaluated as 141 cm^2 and the masses were 8.7 and 0.62 g, respectively.

3 Results and discussion

3.1 Voltammetric measurements

Electrochemical reactions were studied by cyclic voltammetry with different electrode materials (Pt, Au, glassy C and 316L stainless steel), at T = 25 °C. Cyclic voltammograms were carried out at a sweep rate of 50 mV s^{-1}. Cyclic voltammograms were compared in order to identify the capacitive region. In the case of hydroalcoholic solution, the K_2SO_4 concentration allows neglect of transport by migration. When the 316L stainless steel electrode was immersed in the KHT hydroalcoholic solution, the cyclic voltammogram showed different anodic and cathodic peaks. In order to identify oxidation and reduction waves, the KHT and ethanol concentrations were varied. When an anodic sweep was carried out, two waves were observed at 0 V and +1.2 V (vs. Ag/AgCl/saturated KCl). The first was assigned to the formation of an oxide layer preventing corrosion phenomenon and explains the absence of proportionality between the current intensity and ethanol and KHT concentrations. At high anodic potentials, ethanol was oxidized and the reaction was not reversible. When the cathodic sweeping was carried out, two cathodic waves took place at 0 and +0.4 V (vs. Ag/AgCl/saturated KCl). Another cathodic wave was observed at −0.6 V (vs. Ag/AgCl/saturated KCl) and identified as the proton reduction coming from the hydrogen tartratre anion (TH^-). In the case of the glassy carbon electrode, solvent oxidation and reduction started respectively at +1.5 V and at −1.5 V (vs. Ag/AgCl/saturated KCl) and only the proton reduction was observed at −1.2 V (vs. Ag/AgCl/saturated KCl). On the Pt electrode, three anodic waves were observed during anodic sweep and assigned to ethanol oxidation. Ethanol oxidation on Pt electrodes and the main products observed during its electrochemical oxidation are acetaldehyde, acetic acid and carbon dioxide have been reported [40]. Different hypotheses were involved to explain the mechanism. In the cathodic direction, proton reduction was observed at −0.6 V (vs. Ag/AgCl/saturated KCl). For the Au electrode, one anodic wave was observed at +1.2 V (vs. Ag/AgCl/saturated KCl), in which Au and moderated ethanol oxidation in acid medium are involved. Also two cathodic waves were observed at +0.65 V and −1 V (vs. Ag/AgCl/saturated KCl). The first cathodic peak was identified as Au hydroxide reduction and the second as proton reduction.

It is important to note that proton reduction is observed on all electrodes at smaller potentials. In agreement with previous studies, proton reduction involves a chemical–electrochemical mechanism. Reaction mechanisms have already been studied under different conditions [41–51] and it was shown that no proton diffuses toward the electrode surface; on the contrary, it is the weak acid that releases the weak base [51]. The dehydrogenation stage of TH^- is very fast and the electrochemical reaction is controlled by the electron transfer rate.

For the purposes of this work, the capacitive range of the 316L stainless steel–hydroalcoholic solution interface was evaluated to be −0.7 to +1 V (vs. Ag/AgCl/saturated KCl).

3.2 Contact angle measurements

The wettability behaviour of 316L stainless steel flat and rough surfaces with the three electrolytic solutions from contact angle measurements was achieved without and with the presence of an electrical potential.

The apparent contact angles, θ, between the liquid and solid phases were determined from the analysis of the profile of 10 drops using Eq. 1:

$$\cos\theta = \frac{1 - \left(\frac{h}{r_g}\right)^2}{1 + \left(\frac{h}{r_g}\right)^2} \quad (1)$$

where h is the height and r_g the radius of the drop.

A volume of 6 μL of electrolyte solution was chosen based on Bond number (B_o) evaluation, to form stable droplets, where the effects of gravity are negliglible with respect to surface tension forces ($B_o < 1$):

$$B_o = \frac{\Delta\rho g d_g^2}{4\gamma_i} \quad (2)$$

where $\Delta\rho$ is the difference between the densities of the droplet and air, g is the gravitational constant, d_g is the diameter of the drop and γ_l is the surface tension of the liquid.

In order to exclude other exterior physical phenomena in measurements of the contact angle, the equilibrium state between the liquid and the solid was determined for all electrolytes on two types of metal surface (smooth and rough). For 10 drops, the spreading dynamics of droplets on flat surfaces was studied by measuring the contact angle

evolution until the equilibrium state. The variations of the contact angle and contact line versus time were measured. Three periods of spreading were observed. During the first seconds, a spontaneous spreading of droplets occurred on the metal surface due to the dissipation of energy, viscous forces and physical phenomena [52–57]. Later, the contact angle at the liquid–solid–vapour interface exhibited a constant value that can be interpreted as an equilibrium state at the temperature and pressure of the experiment. And at the end, the contact line was pinned and the evaporation of the drop only took place by the reduction of the contact angle even changing the contact line. Thus, the variation of contact angles for each formed interface as a function of the applied potential from −1.7 to +1.2 V (vs. Ag/AgCl/saturated KCl) was obtained. The potential at open circuit was determined to be equal to +0.2 V (vs. Ag/AgCl/saturated KCl). The wetting behaviour of solid substrates was affected by the nature of the compounds in solution, when a potential was applied, significant changes of contact angles were observed.

The interfacial energy of the 316L stainless steel-aqueous NaF solution system as a function of the applied potential is shown in Fig. 2. These curves have characteristic parabolic shapes, where the maxima can be observed near a potential of 0 V and +0.5 V (vs. Ag/AgCl/saturated KCl), and may be assimilated to electrocapillary curves. Wettability was simulated from the Lippmann-Young equation

$$\cos\theta^{E} = \cos\theta^{o} - \frac{\varepsilon_o \varepsilon (E_o + E)^2}{2\gamma_{sl}\delta} \tag{3}$$

where ε_o is the vacuum permittivity, ε the liquid permittivity, E_o the open circuit potential, E the applied potential, γ_{sl} the vapour–liquid surface tension and δ the thickness of the electrochemical double layer.

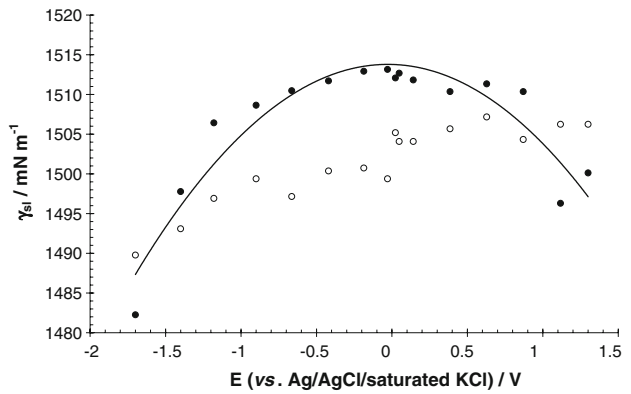

Fig. 2 Electrocapillary curve for the 5×10^{-3} M NaF aqueous solution–316L stainless steel interface. The line is the fit of the electrocapillary curve using the Young-Lippmann model (Eq. 3). The empty circles represent the solution–smooth surface interface. The filled circles represent the solution–rough surface interface

The surface charge and capacitance were estimated from the first and second derivatives of Lippmann equation, respectively.

In the case of NaF aqueous solution–316L stainlees steel interfaces, the simulations give good correlations between theoretical and experimental values. This allows estimation of, for the rough surface, an interface capacitance of 0.22 μF cm^{-2}, a thickness of the electrochemical double layer equal to 0.1 nm and a maximum of the curve that can be assimilated to the potential of zero charge (pzc) at −0.029 V (vs. Ag/AgCl/saturated KCl), assuming the double layer is a condenser of constant capacity. For the smooth surface, the experimental data do not allow a maximum to be found because of a constant increase of the interfacial energy with potential.

For KHT aqueous solution–316L stainless steel interfaces, the values of solid–liquid interfacial energies are lower than those obtained with the NaF aqueous solution (Fig. 3). In this case, KHT modifies the intermolecular forces in water and the hydrophilic properties of the interface seem to be improved. It may be supposed that hydrocarbon chains of theTH^{-} ions are oriented towards the liquid phase in order to diminish the hydrophobic forces. In addition, the electrocapillary curves show that the observed behaviours are different from those predicted by Eq. 3. However, the metal–solution interfacal energy changes slightly with potential. In both cases, the interfacial energies diminish with the increase in potential and there are important variations of interfacial energies at potentials near 0 V (vs. Ag/AgCl/saturated KCl), where a marked minimum is noted in the two cases. Even though similar behaviours are obtained, the topography of the surface has a clear effect on interfacial energies.

Figure 4 shows the wettability curves of 316L stainless steel surfaces with the KHT hydroalcoholic solution. It must be noted that two electrocapillary curves were

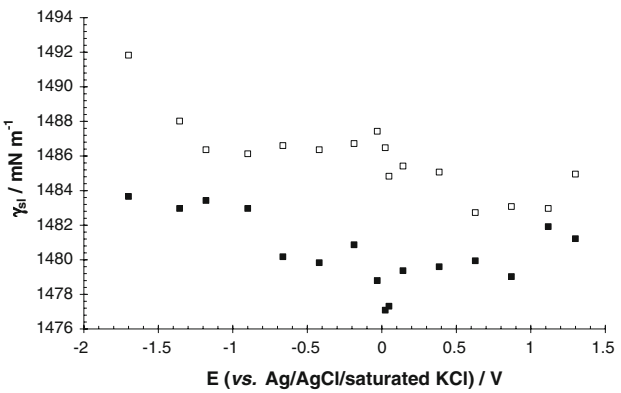

Fig. 3 Electrocapillary curve for the 12.8×10^{-3} M KHT aqueous solution–316L stainless steel interface. The empty squares represent the solution–smooth surface interface. The filled squares represent the solution–rough surface interface

superimposed; the type of surfaces has no influence on interfacial energies. This behaviour was corroborated when the wettability study was carried out by using the captive bubble method (results not shown). These interfaces present lower interfacial energies than in the other cases. This may be due to the adsorption of ethanol molecules at the solid–liquid interface as reported in the past. However, on both sides of wettability curves, it is possible to observe the influence of potential on solid–liquid interfacial energies and especially in the center part that may be influenced by the electrooxidation of the 316L stainless steel surface as cited in the voltammetric study.

In order to clarify the role of the topography of 316L stainless steel surfaces on observed electrocapillarity, the liquid–solid contact line (L_{sl}) associated with local surface defects [58] was studied. The experimental approach consisted in measuring the contact line of drops as a function of potential. In the case of the NaF solution–rough surface interface, the contact line lengthens with potential according to Eq. 6:

$$\gamma_l \frac{dA_{lv}}{dE} = (\gamma_{sl} - \gamma_s)\frac{dA_{sl}}{dE} = \frac{\varepsilon\varepsilon_o}{\delta}E \tag{4}$$

$$A_{sl}|_{E_o}^{E} = \frac{C_d}{2(\gamma_{sl} - \gamma_s)}\Delta E^2 \tag{5}$$

and thus:

$$L_{sl}|_E = L_{sl}|_{Eo} + \left(\frac{2C_d}{\pi(\gamma_{sl} - \gamma_s)}\right)^{1/2}\Delta E^2 \tag{6}$$

where A_{lv} and A_{sl} are the surface areas of the liquid–vapour and solid–liquid interfaces, respectively.

The analysis of this study shows that the standard deviation of contact angles for each system may be due to contact angle hysteresis ($\Delta\theta$), which can arise from molecular interactions between liquid and solid or from surface anomalies (roughness or heterogeneities). For NaF aqueous solution–316L stainless steel system, the difference between these contact angles may be explained by Cassie's model which assumes that between the solid and the liquid, air layers are trapped in the valleys of the roughness causing more elevated contact angles [59]. For drops of KHT aqueous solution on smooth and rough surfaces, the contact line seems to shorten slightly when the potential increases. In the case of the rough surface, this phenomenon is undoubtedly explained by the Wenzel model where the drop collapses completely over the asperities [60]. When the KHT hydroalcoholic solution was used, it was difficult to establish the topography effect. Therefore, the roughness hypothesis cannot be used since other phenomena may be present; for instance, aliphatic alcohols tend to form monolayers of well oriented molecules at the water surface (even below their solubility in water).

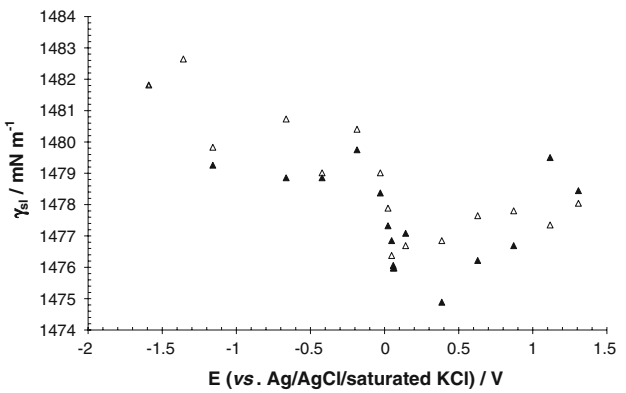

Fig. 4 Electrocapillary curves for the KHT hydroalcoholic solution–316L stainless steel interface. The electrolytic solution contains 12.8×10^{-3} M KHT and 1.15×10^{-3} M K_2SO_4 in 12% vol. ethanol. The empty triangles represent the solution–smooth surface interface. The filled triangles represent the solution–rough surface interface

3.3 Capillary rise measurements

This method is an important way to determine contact angles in metallic porous materials. The wettability studies were carried out by measuring the rate at which a liquid rises into the porous medium. At the early stages, the variation of the mass of liquid is linear and tends toward a constant value which may be considered as an equilibrium state.

The model used for calculating the equilibrium state assimilates the 316L stainless steel material to the capillary tubes. Thus, the mass, W, in the porous material was estimated by a modified Jurin equation

$$W = \frac{4\pi r\gamma_l \cos\theta}{g} \tag{7}$$

The dynamic absorption of the liquid solution into the porous material was achieved during ten experiments, in the same conditions, to determine the average capillary radius, r, the contact angle, θ, and to verify the reproducibility. Moreover, the dynamics of capillary rise was evaluated by the Washburn equation [61]:

$$h\frac{dh}{dt} = \frac{r\gamma_l}{2\mu}\cos\theta \tag{8}$$

where h is the height of the meniscus and μ is the dynamic viscosity of the liquid.

In the kinetics of the capillary flow, inertia, surface tension, hydrostatic pressure, viscous and gravitational forces are involved. Experimental data show that the viscous brake is proportional to the ascension rate of fluid and to the distance of impregnation.

In order to observe the influence of potential on the mass of hydroalcoholic solution at equilibrium, the capillary

material was used as one of the electrodes of a cell of the chain symbolic system PtCu|(5 × 10^{-3} M) $Cu^{2+}SO_4^{2-}$, pH = 1|CuPt, and a potential difference, ΔE, was applied between two Pt electrodes covered by copper. The relative potential of the capillary structure was determined with respect to Ag/AgCl/saturated KCl reference electrode in contact with the copper sulphate solution. During these experiments, the potential was maintained constant. Some results plotted in Fig. 5 show the early instants of the dynamics of the capillary rise obtained with different values of potential. Here, it is possible to observe the influence of applied potential on the mass of absorbed hydroalcoholic solution. Although capillary behaviours follow the Washburn equation closely when a static contact angle is associated, the deviations between experiment and theoretical data may be due to non-static contact angles. At equilibrium, the mass of absorbed hydroalcoholic solution into the metallic porous structure as a function of potential goes through a maximum at −0.212 V (vs. Ag/AgCl/saturated KCl). In addition, the height of the meniscus is proportional to the square of the potential and is independent of the surface tension of the liquid, between +0.65 and −0.2 V (vs. Ag/AgCl/saturated KCl), as described by Eq. 9:

$$\Delta h = \frac{C_d E^2}{\rho g r} \tag{9}$$

where Δh is the height difference.

However, interfacial energies fall at higher cathodic potentials, which may be linked to the electroreduction of H^+coming from TH^- ions on the 316L stainless steel surface.

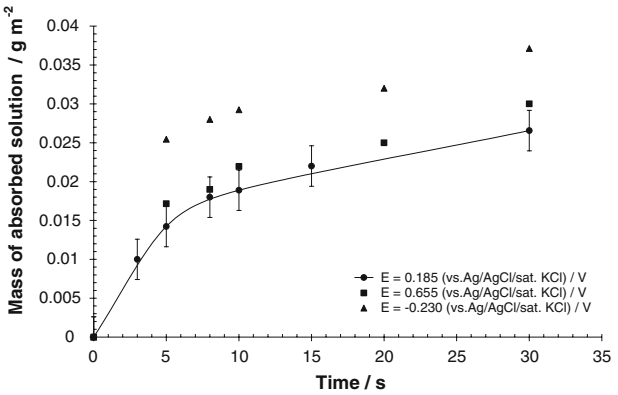

Fig. 5 Influence of potential on the dynamic behaviour of capillary rise

3.4 KHT crystallization

In this part, several types of experiments of KHT crystallization on 316L stainless steel surfaces (plate or wires) without or with an electrical potential were carried out in order to study the influence of potential on the formation of KHT crystals on the metal surface by heterogeneous nucleation.

Experiments on KHT crystallization by evaporation of drops of supersaturated hydroalcoholic solutions (S = 1.69) were carried out. Figure 6 shows four images of KHT crystals obtained on the metal surface in the absence and in the presence of a potential. When potential is applied, a more regular presence of small KHT crystals at the periphery of the hydroalcoholic solution drop is noted. This seems to indicate that the potential influences KHT nucleation at the metal substrate–liquid–air interface. The morphology of KHT crystals is similar to that reported early [7–9].

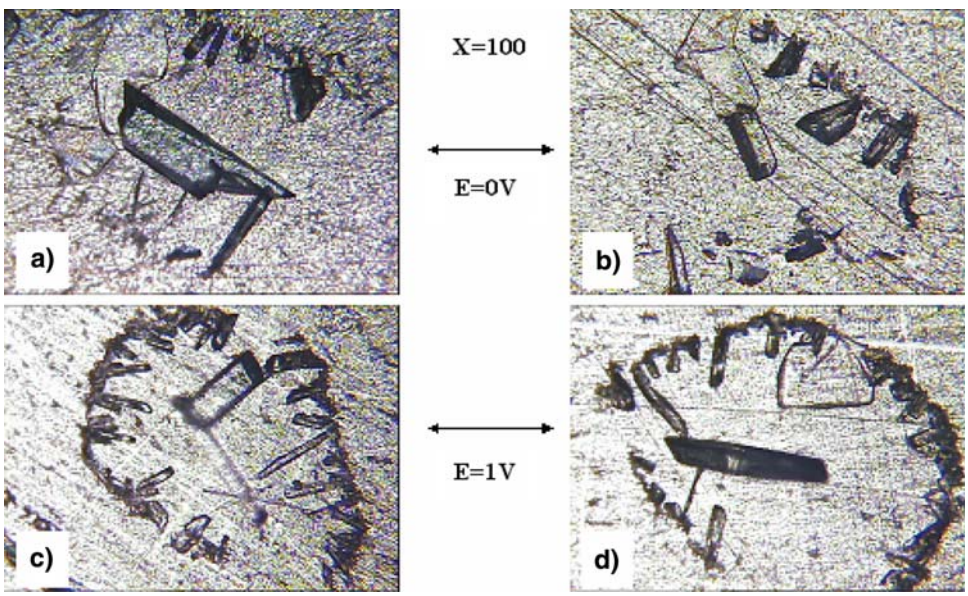

Fig. 6 Images of KHT crystals formed from hydroalcoholic solution drops **a**, **b** in the absence and **c**, **d** in the presence of potential (E = + 1 V) on 316L stainless steel surface

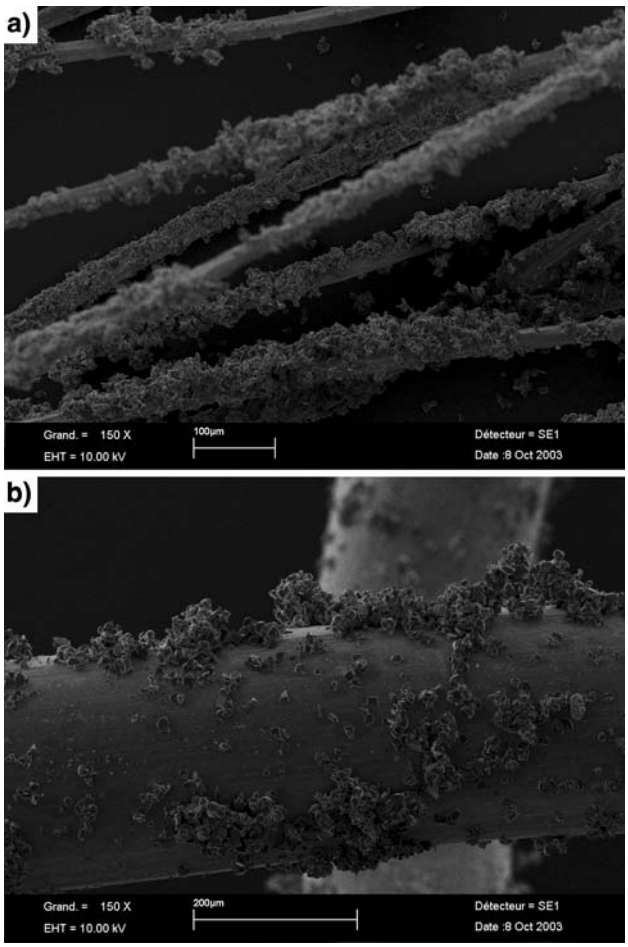

Fig. 7 MEB images of PB and PF stainless steel wires **a** completely and **b** partially covered by KHT crystals, respectively

When a flat plate was immersed in a supersaturated aqueous or hydroalcoholic solution, KHT monocrystals formed on a square surface of 0.76 cm^2 were counted and measured. At anodic potentials, the average size of KHT monocrystals from both supersaturated solutions shows no significant variation; the average sizes of the KHT crystals are 33 and 25 µm, from aqueous and hydroalcoholic solutions, respectively. However, when high cathodic potentials, $E < -0.5$ V (vs. Ag/AgCl/saturated KCl), were applied, the average size of KHT crystals (45 µm for the KHT aqueous solution) increased and the number of formed monocrystals decreased significantly. In fact, at these cathodic potentials, the TH^- ion concentration may be maintained constant near the 316L stainless steel surface by diffusion and thus crystal growth is enhanced. In contrast, the number of KHT monocrystals on a 316L stainless steel surface was higher when anodic potentials were used. In the hydroalcoholic solution, crystal growth was more limited than in the aqueous solution. The adsorption of ethanol molecules on the 316L stainless steel surface may be the origin of the inhibition of KHT crystallization on the surface. This phenomenon seems to be in opposition to the fact that KHT solubility decreases with increase in ethanol mole fraction.

When KHT crystallization was carried out on both 316L stainless steel wires of different diameters (PF and PB), KHT crystals adhered better on the PB wires than on the PF ones (of larger diameter) at open circuit potential. The standard deviation corresponding to ten crystallization tests for each metal grid is 5 times smaller with the PB substrate than with the PF substrate. This comes from the fact that when the PF stainless steel wire grid is removed from the solution, KHT crystals are detached and fall. This phenomenon seems less marked with PB substrate which leaves the solution perfectly limpid and thus gives 66% yield. Figure 7 shows MEB images of PF and PB substrates partially and completely covered by KHT crystals, respectively. According to the microscopic analysis, it appears that, on their surface, PB wires have many cavities which contribute to increased surface area of the 316L stainless steel wire grid and activate the nucleation by seeds in cavities. On the other hand, the mass of KHT crystals increases slightly with potential applied to the PB wire grid (Fig. 8). The standard deviation becomes more

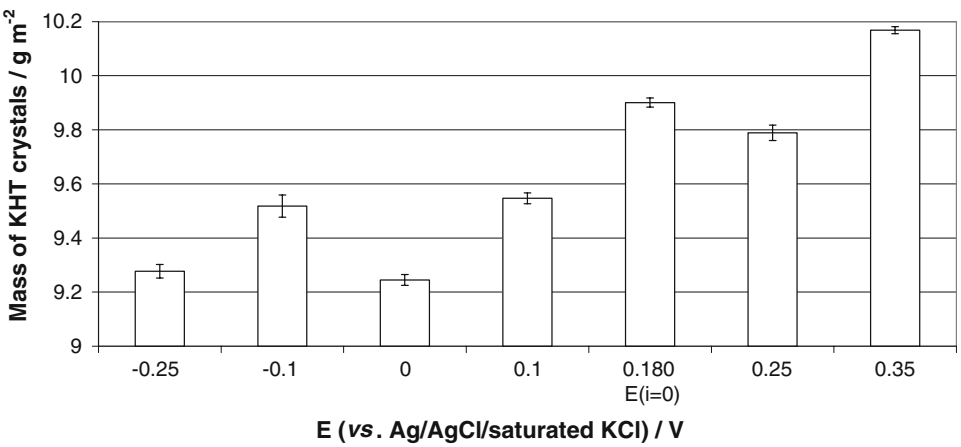

Fig. 8 Influence of potential on the mass of KHT crystals on the PB metal substrate

significant when cathodic potentials are applied. This may be due to both adhesion energy reduction and crystal size.

4 Conclusions

Because molecular and mechanical interactions play a decisive role in nucleation and adhesion phenomena, the experimental strategy employed in this work allowed evaluation of the solid–liquid interfacial energy as a function of potential from contact angle and capillary rise measurements. The solid–liquid interface was examined by cyclic voltammetry. The H^+ reduction is present on all studied electrode materials and takes place at cathodic potentials. Other reactions involve ethanol oxidation to acetaldehyde, acetic acid, etc., and oxidation and reduction of electrode materials.

The spreading of aqueous or hydroalcoholic electrolyte solutions on metal substrates is reached when a potential is applied to the metal substrate. According to the Lippmann-Young equation for electrocapillarity, a parabolic behaviour is obtained for NaF solution. The topography of the solid substrate influences the apparent contact angle in the cases of NaF and KHT aqueous solutions. For the KHT hydroalcoholic solution, the 316L stainless steel topography has no influence on electrocapillary behaviour when ethanol is present in solution; it seems that, at the solid–liquid interface, the formation of a layer of adsorbed ethanol molecules may be at the origin of these results. From the wetting data obtained by capillary rise, the interfacial energy is easily estimated when the liquid and solid surface tensions are independent of the electric potential.

On the other hand, ethanol molecules play a double role: they increase the supersaturation degree in solution and inhibit the formation of KHT crystals on a metal substrate because of their adsorption. This causes a reduction in the number of KHT crystals on the metal substrate. Crystal adhesion on wires of small diameter increases with potential and rugosity.

Acknowledgements Special thanks from the authors to the Consejo Nacional de Ciencia y Tecnologia (CONACyT, México), the Institut Technique de la Vigne et du Vin (ITV, Région Midi-Pyrénées) and Oenodev for financial support for this research.

References

1. Maujean A (1994) In: B Doneche (ed) Les acquisitions récentes dans les traitements physiques du vin. Lavoisier Tec & Doc, Paris
2. Marh GL, Joslyn MA (1935) Ind Eng Chem 27:1252
3. Tanahashi H, Nishino H, Tojo K, Nakai TJ (1992) Chem Eng Jpn 25:342
4. Gerbaud V, Gabas N, Laguerie C, Blouin J, Vidal S, Moutounet M, Pellerin P (1996) Trans I Chem E 74:782
5. Gerbaud V, Gabas N, Blouin J, Laguerie C (1996) J Cryst Growth 166:172
6. Gerbaud V, Gabas N, Blouin J, Pellerin P, Moutounet M (1997) J Int Sci Vigne Vin 31:65
7. Rodriguez-Clemente R, Correa-Gorospe I (1998) Am J Enol Vitic 39:169
8. Sangwal K, Veintemillas-Verdaguer S (1994) Cryst Res Technol 29:639
9. Veintemillas-Verdaguer S, Rodriguez-Clemente R (1999) J Cryst Growth 99:211
10. Favarel JL, Gabas N, Latge C (1998) French patent 97 09719
11. Cambelle AA (1999) Curr Opin Colloid Interface Sci 4:40
12. Hunter KG (1996) Curr Opin Solid State Mater Sci 1:430
13. Wu W, Nancollas HG (1996) J Colloid Interface Sci 182:365
14. Fletcher NH (1958) J Chem Phys 29:572
15. Kimble WL, Paxton TE, Rousseau RW, Sabanis A (1998) J Cryst Growth 187:268
16. Liu Y, Wu W, Sethuraman G, Nancollas GH (1997) J Cryst Growth 174:386
17. Nancollas GH, Wu W (2000) J Cryst Growth 211:137
18. Paxton TE, Sambanis A, Rousseau RW (1999) J Cryst Growth 198/199:656
19. Turnbull D, Vonnegut B (1952) Ind Eng Chem 44:1292
20. Turnbull DJ (1950) Chem Phys 18:198
21. Volmer M (1929) Z Electrochem 35:555
22. Wu W, Nancollas GH (1999) Adv Colloid Surf A 79:229
23. Rieke PC (1997) J Cryst Growth 182:472
24. Wu W, Zhuang H, Nancollas GH (1997) J Biomed Mater Res 35:93
25. Wu W, Nancollas GH (1998) J Colloid Interface Sci 199:206
26. Campbell AA, Fryxell GE, Linehan LC, Graff GL (1996) J Biomed Mater Res 32:111
27. Heywood BR, Mann S (1994) Chem Mater 6:311
28. Lui J, Kim AT, Wang LG, Palmer BJ, Chen YL, Brunsma P, Bunker BC, Exharos GJ, Graff GL, Rieke PC (1996) Adv Colloid Interface Sci 69:131
29. Mann S, Heywood BR, Rajam S, Walker JB (1991) J Phys D Appl Phys 24:154
30. Lippmann G (1875) Ann Chim Phys 5:494
31. Frumkin A, Gorodetzkaja A (1928) Z Phys Chem 136:451
32. Berry S, Kedzierski J, Abedian B (2007) Langmuir 23:12429
33. Bienia M, Quilliet C, Vallade M (2003) Langmuir 19:9328
34. Divilov R (2000) Langmuir 16:6719
35. Kang KH (2002) Langmuir 18:10318
36. Lin L Jr, Lee GB, Chang YH, Lien KY (2004) Langmuir 22:484
37. Quilliet C, Berge B (2001) Curr Opin Colloid Interface Sci 6:34
38. Vallet M, Vallade M, Berge B (1999) Eur Phys J B 11:583
39. Verheijen HJ, Prins MWJ (1999) Langmuir 15:6616
40. Lamy C, Belgsier E, Léger LM (2001) J Appl Electrochem 31:799
41. Lamy-Pirata E, El Mouahid S, Bardier J (2000) Electrochim Acta 45:4299
42. Jaworski A, Donten M, Stojek Z, Osteryoung JG (1999) Anal Chem 71:167
43. Daniele S, Baldo MA, Bragato C, Lavagnini I (1998) Anal Chim Acta 361:141
44. Daniele S, Lavagnini I, Baldo MA, Magno F (1998) Anal Chem 70:285
45. Daniele S, Baldo MA, Somonetto F (1996) Anal Chim Acta 331:117
46. Daniele S, Lavagnini I, Baldo MA, Magno F (1996) J Electroanal Chem 404:105
47. Ciszkawska M, Stojek Z (1994) Anal Chem 64:2372
48. Ciszkawska M, Stojek Z, Morris SE, Osteryoung JG (1992) Anal Chem 64:2372
49. Xie Y, Osteryoung JG (1997) J Electroanal Chem 439:163

50. Stojek Z (1994) Anal Chem 66:1507
51. Trémillon B (1993) Electrochimie analytique et réactions en solution, Tome 2. Masson, Paris
52. Extrand CW (2003) Langmuir 19:646
53. Extrand CW (2002) Langmuir 18:7991
54. Seveno D, Ledauphin V, Martic G, Voué M, De Coninck J (2002) Langmuir 18:7496
55. von Bahr M, Tiberg F, Yaminsky V (2001) Colloids Surf A Physicochem Eng Asp 193:85
56. Lelah MD, Marmur A (1981) J Colloid Interface Sci 82:518
57. Tanner LH (1979) J Phys D Appl Phys 12:1473
58. Tadmor R (2004) Langmuir 20:7659
59. Cassie ABD, Baxter S (1944) Trans Faraday Soc 40:546
60. Wenzel RN (1936) Ind Eng Chem 28:988
61. Washburn EW (1921) Phys Rev 3:273